Inorganic Chemistry

Article

pubs.acs.org/IC

Synthesis, Structure, Luminescence, and Magnetic Properties of a Single-Ion Magnet "*mer*"-[Tris(*N*-[(imidazol-4-yl)-methylidene]-DL-phenylalaninato)terbium(III) and Related "*fac*"-DL-Alaninato Derivative

Suguru Yamauchi,[†] Takeshi Fujinami,[†] Naohide Matsumoto,*[,†] Naotaka Mochida,[‡] Takayuki Ishida,*[,‡] Yukinari Sunatsuki,[§] Masayuki Watanabe,[∥] Masanobu Tsuchimoto,[⊥] Cecilia Coletti,[#] and Nazzareno Re[#]

[†]Department of Chemistry, Faculty of Science, Kumamoto University, Kumamoto 860-8555, Japan

[‡]Department of Engineering Science, The University of Electro-Communications, Chofu, Tokyo 182-8585, Japan

[§]Department of Chemistry, Faculty of Science, Okayama University, Tsushima-naka 3-1-1, Okayama 700-8530, Japan

[∥]Nuclear Science and Engineering Directorate, Japan Atomic Energy Agency, Tokai-mura 319-1195, Japan

[⊥]Department of Chemistry, Chiba Institute of Technology, Shibazono 2-1-1, Narashino, Chiba 275-0023, Japan

[#]Dipartimento di Farmacia, Universita degli Studi "G.D'Annunzio", I-66100 Chieti, Italy

Supporting Information

ABSTRACT: Two Tb^{III} complexes with the same N_6O_3 donor atoms but different coordination geometries, "*fac*"-$[Tb^{III}(HL^{DL\text{-}ala})_3]\cdot 7H_2O$ (**1**) and "*mer*"-$[Tb^{III}(HL^{DL\text{-}phe})_3]\cdot 7H_2O$ (**2**), were synthesized, where $H_2L^{DL\text{-}ala}$ and $H_2L^{DL\text{-}phe}$ are *N*-[(imidazol-4-yl)methylidene]-DL-alanine and -DL-phenylalanine, respectively. Each Tb^{III} ion is coordinated by three electronically mononegative NNO tridentate ligands to form a coordination geometry of a tricapped trigonal prism. Compound **1** consists of enantiomers "*fac*"-$[Tb^{III}(HL^{D\text{-}ala})_3]$ and "*fac*"-$[Tb^{III}(HL^{L\text{-}ala})_3]$, while **2** consists of "*mer*"-$[Tb^{III}(HL^{D\text{-}phe})_2(HL^{L\text{-}phe})]$ and "*mer*"-$[Tb^{III}(HL^{D\text{-}phe})(HL^{L\text{-}phe})_2]$. Magnetic data were analyzed by a spin Hamiltonian including the crystal field effect on the Tb^{III} ion ($4f^8$, $J = 6$, $S = 3$, $L = 3$, $g_J = 3/2$, $^7F_6$). The Stark splitting of the ground state $^7F_6$ was evaluated from magnetic analysis, and the energy diagram pattern indicated easy-plane and easy-axis (Ising type) magnetic anisotropies for **1** and **2**, respectively. Highly efficient luminescences with $\Phi = 0.50$ and 0.61 for **1** and **2**, respectively, were observed, and the luminescence fine structure due to the $^5D_4 \rightarrow {}^7F_6$ transition is in good accordance with the energy diagram determined from magnetic analysis. The energy diagram of **1** shows an approximate single-well potential curve, whereas that of **2** shows a double- or quadruple-well potential within the $^7F_6$ multiplets. Complex **2** displayed an onset of the out-of-phase signal in alternating current (ac) susceptibility at a direct current bias field of 1000 Oe on cooling down to 1.9 K. A slight frequency dependence was recorded around 2 K. On the other hand, **1** did not show any meaningful out-of-phase ac susceptibility. Pulsed-field magnetizations of **1** and **2** were measured below 1.6 K, and only **2** exhibited magnetic hysteresis. This finding agrees well with the energy diagram pattern from crystal field calculation on **1** and **2**. DFT calculation allowed us to estimate the negative charge distribution around the Tb^{III} ion, giving a rationale to the different magnetic anisotropies of **1** and **2**.

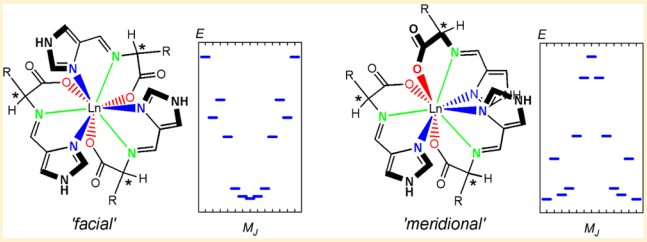

INTRODUCTION

Since the discovery of single-molecule magnets (SMMs) from a Mn_{12} cluster,[1] studies on SMMs consisting of a d element have greatly progressed.[2] During the last decade, lanthanide complexes[3] and lanthanide−transition metal complexes[4] have been extensively studied, because the easy-axis magnetic anisotropy required for a SMM can be given by the electronic structure of the lanthanide ion. There have been many reports on mononuclear[5] and polynuclear[6] lanthanide complexes exhibiting slow relaxation of the magnetization with a relatively large energy barrier. For polynuclear lanthanide complexes,[6] it is difficult to prescribe the molecular design due to the f−f exchange coupling in addition to the crystal-field (CF) effect on the lanthanide ion. For mononuclear lanthanide complexes,[5] SMM behavior is attributed to the CF splitting of the lowest J multiplet. A desirable CF would affect the splitting of the ground J multiplet and give the lowest sublevels with a large $|J_z|$ value and significant energy gap from excited sublevels, thus achieving easy-axis magnetic anisotropy. Therefore, for the purpose of molecular design of SMMs and single-ion magnets (SIMs) with high blocking temperatures and large relaxation

Received: January 22, 2014
Published: June 3, 2014

   dx.doi.org/10.1021/ic5001599 | *Inorg. Chem.* 2014, 53, 5961−5971

barriers, it is essential to establish the correlation between the CF effect and the ground state splitting.

In our previous paper we reported the synthesis, structure, and luminescent properties of mononuclear Eu^{III} complexes "*fac*"-$[Eu^{III}(HL^{DL\text{-}ala})_3]\cdot 8H_2O$ and "*mer*"-$[Eu^{III}(HL^{DL\text{-}phe})_3]\cdot 8H_2O$,[7] in which $H_2L^{DL\text{-}ala}$ denotes *N*-[(imidazol-4-yl)-methylidene]-DL-alanine of a racemic mixture from $H_2L^{D\text{-}ala}$ and $H_2L^{L\text{-}ala}$ and $H_2L^{DL\text{-}phe}$ similarly denotes racemic *N*-[(imidazol-4-yl)methylidene]-DL-phenylalanine. Eu^{III} complexes coordinated by three mononegative tridentate ligands ($HL^{DL\text{-}ala}$ or $HL^{DL\text{-}phe}$) have nine coordination with N_6O_3 donor atoms but two different coordination geometries, "*fac*"-$[Eu^{III}(HL^{DL\text{-}ala})_3]$ and "*mer*"-$[Eu^{III}(HL^{DL\text{-}phe})_3]$, as shown in Scheme 1. These Eu^{III} complexes displayed sharp emission bands assigned to the f−f transitions by excitation with high quantum yields (Φ = 0.25 and 0.30) and showed a different emission pattern demonstrating the different Stark splitting due to their different "*fac*"- and "*mer*"-coordination geometries.

Scheme 1. "Facial" and "Meridional" Geometries of Lanthanide(III) (Ln) Complexes Coordinated by Three Tridentate Ligands H_2L^{aa}, "*fac*"-$[Ln^{III}(HL^{aa})_3]$ and "*mer*"-$[Ln^{III}(HL^{aa})_3]$[a]

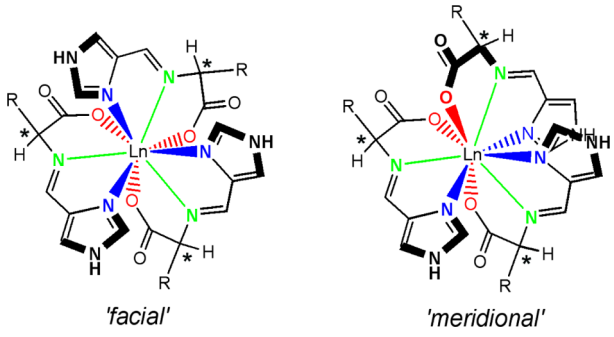

[a]aa stands for an amino acid used in a Schiff base H_2L. According to the IUPAC rule, *fac* and *mer* only apply to six-coordinated octahedral complexes. "*fac*" and "*mer*" are used for nona-coordinated complex in this text.

In this study, the Tb^{III} complexes "*fac*"-$[Tb^{III}(HL^{DL\text{-}ala})_3]\cdot 7H_2O$ (**1**) and "*mer*"-$[Tb^{III}(HL^{DL\text{-}phe})_3]\cdot 7H_2O$ (**2**), which have structures isomorphous to those of the corresponding Eu^{III} complexes, have been synthesized, and their structures, magnetic, and luminescent properties and DFT calculations have been investigated. The ground state of the Tb^{III} ion is $^7F_6$ ($4f^8$, J = 6, S = 3, L = 3, g_J = 3/2, $^7F_6$), and the CF effect on the Tb^{III} ion removes the degeneracy of the 13 components, $|J, J_z\rangle = |6, J_z\rangle$ ($J_z = \pm 6, \pm 5, \pm 4, \pm 3, \pm 2, \pm 1, 0$), of the $^7F_6$ ground state (known as the Stark splitting). The energy level patterns and the nature of the corresponding anisotropy, easy axis (Ising type) or easy plane, depend on the CF generated by the distribution of coordination donor atoms around the Tb^{III} ion. The present "*fac*"- and "*mer*"-Tb^{III} complexes are suitable compounds to investigate the relation among the coordination geometry, negative charge distribution around the lanthanide ion, and energy diagram of the ground state on one side and the dc and ac magnetic properties including SIM behavior on the other side. The temperature dependence of the magnetic susceptibilities and field-dependent magnetization were measured, and magnetic data were analyzed by a spin Hamiltonian including the CF effect on the Tb^{III} ion. The best-fit parameters from magnetic analyses gave the energy diagrams for the Stark splitting of the ground state $^7F_6$, which were compared with the emission spectrum of the f−f transition. Actually, emission spectroscopy is indispensable to verify the energy level structure regulated by the CF. DFT calculation allowed us to estimate the negative charge distribution around the Tb^{III} ion and give a rationale for the different behavior of the "*fac*" and "*mer*" forms. Alternating current (ac) susceptibility measurements demonstrated for **2**, but not for **1**, an out-of-phase signal with frequency dependence, indicative of SIM. Finally, magnetic hysteresis of **2** was recorded in the pulsed-field magnetization measurements. We report here the synthesis, structures, luminescent and magnetic properties, and DFT calculations of **1** and **2**.

EXPERIMENTAL SECTION

Materials. All reagents and solvents in the syntheses were of reagent grade, available from Tokyo Kasei Co., Ltd. and Wako Pure Chemical Industries, Ltd. These were used without further purification. All reactions were carried out under ambient atmosphere.

$H_2L^{DL\text{-}ala}$ and $H_2L^{DL\text{-}phe}$. *N*-[(Imidazol-4-yl)methylidene]-DL-alanine (abbreviated as $H_2L^{DL\text{-}ala}$) and *N*-[(imidazol-4-yl)methylidene]-DL-phenylalanine (abbreviated as $H_2L^{DL\text{-}phe}$) were prepared by 1:1 condensation reactions of 4-formylimidazole and DL-alanine and DL-phenylalanine, respectively, according to the method reported previously.[8] The resultant ligands were not isolated and used for the syntheses of Tb^{III} complexes.

"*fac*"-$[Tb^{III}(HL^{DL\text{-}ala})_3]\cdot 7H_2O$ (1). To the resultant ligand solution of $H_2L^{DL\text{-}ala}$ (1.5 mmol) in 10 mL of methanol was added a solution of terbium(III) acetate tetrahydrate (0.5 mmol, 0.204 g) in 5 mL of water at room temperature. The mixture was stirred for 10 min and then filtered. A diffusion method was applied for crystallization; a vessel of the filtrate was left to stand for several days in a desiccator that is saturated by vapor of acetone, during which time colorless block crystals precipitated. They were collected by suction filtration. Yield: 0.340 g (43%). Anal. Calcd for $[Tb^{III}(HL^{DL\text{-}ala})_3]\cdot 7H_2O$, $C_{21}H_{24}N_9O_6Tb\cdot 7H_2O$: C, 32.19; H, 4.89; N, 16.09. Found: C, 32.29; H, 4.57; N, 15.85. IR (KBr, cm^{-1}): ν(C=N) 1645, $\nu_a(COO^-)$ 1585, $\nu s(COO^-)$ 1410. TGA (Figure S1, Supporting Information): 18% weight loss was observed in the heating mode from room temperature to 150 °C. In the cooling mode, the sample absorps the vapor to increase the weight from −18% to −2.5%.

"*mer*"-$[Tb^{III}(HL^{DL\text{-}phe})_3]\cdot 7H_2O$ (2). To the resultant ligand solution of $H_2L^{DL\text{-}phe}$ (1.5 mmol) in 10 mL of methanol was added a solution of terbium(III) acetate tetrahydrate (0.5 mmol, 0.204 g) in 5 mL of water at room temperature. The mixture was stirred for 10 min and filtered. For crystallization, a diffusion method was applied: A vessel of the filtrate was left to stand for several days in a desiccator that is saturated by a vapor of acetone, during which time colorless block crystals precipitated. Yield: 0.577 g (57%). Anal. Calcd for $[Tb^{III}(HL^{DL\text{-}phe})_3]\cdot 7H_2O$, $C_{39}H_{36}N_9O_6Tb\cdot 7H_2O$: C, 46.30; H, 4.98; N, 12.46. Found: C, 46.42; H, 5.10; N, 12.16. IR (KBr, cm^{-1}): ν(C=N) 1643, $\nu_a(COO^-)$ 1595, $\nu s(COO^-)$ 1400. TGA (Figure S2, Supporting Information): 14% weight loss was observed in the heating mode from room temperature to 150 °C. In the cooling mode, the sample absorps the vapor to increase the weight from −14% to −9%.

Physical Measurements. Elemental C, H, and N analyses were carried out at the Center for Instrumental Analysis of Kumamoto University. Infrared spectra were recorded at room temperature using a JEOL JIR-6500W spectrometer with samples in KBr disks. Thermogravimetric analyses (TGA) were performed on a TG/DTA6200 (Seiko Instrument Inc.). Samples of ca. 3 mg were heated from room temperature to 150 °C in the heating mode at a heating rate of 5 °C min^{-1}, kept the temperature for 1 h, and then cooled to room temperature. High-resolution luminescence spectra were measured with a Horiba Fluoromax-4P spectrometer at 77 K. A quartz tube (o.d. 8 mm) was used as a powder cell fixed in a quartz dewar sample holder filled with liquid nitrogen. The excitation slit was 1 nm, and the emission slit was 0.2 nm. Quantum yields of **1** and **2** in

dx.doi.org/10.1021/ic5001599 | Inorg. Chem. 2014, 53, 5961−5971

the solid state at room temperature were obtained by an absolute method using a Hitachi F-7000 fluorescence spectrometer equipped with an integrating sphere. Temperature-dependent magnetic susceptibilities in the temperature range 1.9−300 K at an external magnetic field of 0.1 T and field-dependent magnetization measurements in an applied magnetic field from 0 to 5 T at 1.9 K were measured with an MPMS XL5 SQUID susceptometer (Quantum Design, Inc.). All samples were fixed with a small amount of liquid paraffin to avoid orientation in the field. Calibrations were performed with palladium. Corrections for diamagnetism were applied using Pascal's constants.[9] Alternating current magnetic susceptibility was measured on a PPMS ac/dc magnetometer (Quantum Design, Inc.) in a temperature range down to 1.9 K at 0 and 1000 Oe dc fields. Low-temperature magnetization was measured by a conventional inductive probe in pulsed-magnetic fields equipped with a ^{3}He cryostat.[10] The sample was not fixed within the sample tube, and then it was aligned along the magnetic field direction. After we applied the magnetic field several times, the orientation effect was saturated, and the magnetization curves obtained in further shots were found to be identical.

X-ray Crystal Structure Analyses. Single-crystal X-ray diffraction data of **1** and **2** were collected by a Rigaku RAXIS RAPID imaging plate diffractometer using graphite-monochromated Mo Kα radiation (λ = 0.71073 Å) at 103 and 108 K, respectively. The temperature of the crystal was maintained within an accuracy of ±2 K by a Rigaku N_2 cryostat. Structures were solved by direct methods and expanded using the Fourier technique.[11] Hydrogen atoms were located at the calculated positions and refined using a riding model. All calculations were performed using the CrystalStructure crystallographic software package.[12] Crystallographic data and relevant coordination bond distances with hydrogen bond distances are given in Tables 1 and 2, respectively.

Table 1. X-ray Crystallographic Data for "*fac*"-[$Tb^{III}(HL^{DL\text{-}ala})_3$]·8$H_2O$ (1) and "*mer*"-[$Tb^{III}(HL^{DL\text{-}phe})_3$]·8.75$H_2O$ (2)

complex	"*fac*"-[$Tb^{III}(HL^{DL\text{-}ala})_3$]·8$H_2O$ (**1**)	"*mer*"-[$Tb^{III}(HL^{DL\text{-}phe})_3$]·8.75$H_2O$ (**2**)
formula	$C_{21}H_{40}N_9O_{14}Tb$	$C_{39}H_{53.5}N_9O_{14.75}Tb$
fw	801.52	1043.33
T, K	103	108
space group	$R\bar{3}$ (No. 148)	$I4_1/a$ (No. 88)
a, b, Å	13.6473(7)	22.7959(4)
c, Å	29.017(2)	35.2149(7)
V, Å^3	4680.4(5)	18299.5(6)
Z	6	16
D_{calcd}, g cm^{-3}	1.706	1.515
μ, cm^{-1}	23.409	16.175
R,[a] R_w[b]	0.0621, 0.1720	0.0678, 0.1908

[a] $R = \Sigma||F_o| - |F_c||/\Sigma|F_o|$. [b] $R_w = [\Sigma w(F_o^2 - F_c^2)^2/\Sigma w(F_o^2)^2]^{1/2}$.

DFT Calculations. DFT (density functional theory) unrestricted calculations were performed with the Jaguar 7.9 quantum chemistry package[13] using B3LYP-D3, i.e., B3LYP functional with Grimme's ab initio long-range dispersion corrections.[14] This functional is known to give good performance at a reasonable computational cost for the description of large systems, where noncovalent interactions may play an important role, generally dealt with heavy highly correlated techniques. A Cundari-Stevens ECP basis set,[15] also named csdz, was employed for terbium. This set provides a good description for lanthanides using an effective core potential for the inner core electrons and treating outer core and valence electrons with a 4s/4p/2d/2f basis set. Main group atoms were described by a 6-31G(p) basis set.

Table 2. Relevant Coordination Bond Distances, Angles, and Hydrogen Bond Distances for 1 and 2[a]

	bond length (Å)		
1	Tb−O(1) 2.373(5)	Tb−N(2) 2.555(7)	Tb−N(3) 2.552(8)
2	Tb−O(1) 2.364(4)	Tb−N(2) 2.569(5)	Tb−N(3) 2.517(5)
	Tb−O(3) 2.422(4)	Tb−N(5) 2.534(5)	Tb−N(6) 2.551(5)
	Tb−O(5) 2.434(4)	Tb−N(8) 2.535(5)	Tb−N(9) 2.555(5)
	bond angle (deg)		
1	O(1)−Tb−N(2) 128.6(3)	O(1)−Tb−N(3) 64.3(2)	N(2)−Tb−N(3) 64.3(2)
2	O(1)−Tb−N(2) 127.48(13)	O(1)−Tb−N(3) 65.09(13)	N(2)−Tb−N(3) 65.06(14)
	O(3)−Tb−N(5) 126.12(14)	O(3)−Tb−N(6) 63.09(13)	N(5)−Tb−N(6) 64.33(14)
	O(5)−Tb−N(8) 121.36(13)	O(5)−Tb−N(9) 62.52(13)	N(8)−Tb−N(9) 65.32(15)
1	O(1)−Tb−O(1)*1 77.30(19)	N(2)−Tb−N(2)*1 80.4(2)	N(3)−Tb−N(3)*1 120.00(18)
2	O(1)−Tb−N(5) 88.43(13)	N(2)−Tb−O(3) 66.71(13)	N(3)−Tb−N(6) 123.29(14)
	O(1)−Tb−O(5) 71.04(12)	N(2)−Tb−N(8) 75.36(14)	N(3)−Tb−N(9) 102.05(14)
	O(5)−Tb−N(5) 73.18(13)	O(3)−Tb−N(8) 86.28(14)	N(6)−Tb−N(9) 134.66(14)
	hydrogen bond (Å)		
1	N(1)···O(4)*2 2.786(10)	O(2)···O(4) 2.691(11)	O(3)···O(4) 2.745(8)
	O(4)···O(5) 2.72(2)	O(5)···O(2)*3 2.68(2)	
2	N(1)···O(5)*4 2.820(6)	N(4)···O(4)*5 2.696(6)	N(7)···O(15) 2.723(7)
	O(2)···O(15) 2.741(6)		

[a] Symmetry operations: (*1) $-y + 1, x - y, z$; (*2) $x + 1/3 - 1, y + 2/3 - 1, z + 2/3 - 1$; (*3) $-x + 2/3 + 1, -y + 1/3 + 1, z + 1/3 + 1$; (*4) $-y + 3/4, x + 1/4-1, z + 1/4$; (*5) $y + 3/4, -x + 3/4, z + 3/4 - 1$.

RESULTS AND DISCUSSION

Synthesis and Characterization of "*fac*"-[$Tb^{III}(HL^{DL\text{-}ala})_3$]·7$H_2O$ (1) and "*mer*"-[$Tb^{III}(HL^{DL\text{-}phe})_3$]·7$H_2O$ (2). Two racemic tridentate ligands, *N*-[(imidazol-4-yl)-methylidene]-DL-alanine ($H_2L^{DL\text{-}ala}$) and *N*-[(imidazol-4-yl)-methylidene]-DL-phenylalanine ($H_2L^{DL\text{-}phe}$), were synthesized by 1:1 condensation reactions of 4-formylimidazole and DL-alanine and DL-phenylalanine according to the method reported previously.[8] Such ligand $H_2L^{DL\text{-}ala}$ or $H_2L^{DL\text{-}phe}$ reacts with terbium(III) acetate tetrahydrate in a 3:1 molar ratio to yield electronically neutral Tb^{III} complexes "*fac*"-[$Tb^{III}(HL^{DL\text{-}ala})_3$]·8$H_2O$ (**1**) and "*mer*"-[$Tb^{III}(HL^{DL\text{-}phe})_3$]·8.75$H_2O$ (**2**) as colorless crystals. Crystals contain crystal waters. Thermogravimetric analyses (TGA) for freshly prepared samples revealed the number of the crystal water. In the heating mode from room temperature to 150 °C, 18% weight loss corresponding to ca. 8 water molecules was observed for **1**. In the cooling mode, the sample absorps the atmospheric moisture amount of 7H_2O to increase the 15.5% weight. C, H, and N elemental analyses agreed with the 7H_2O hydration. For **2**, the weight loss corresponding to ca. 8 water molecules was observed in the heating mode and the 5% weight increase corresponding to 2 water molecules was observed in the cooling mode. C, H, and N elemental analyses agreed with the hydration with 7H_2O. The formulas characterized in the X-ray diffraction study actually are "*fac*"-[$Tb^{III}(HL^{DL\text{-}ala})_3$]·8$H_2O$ and "*mer*"-[$Tb^{III}(HL^{DL\text{-}phe})_3$]·8.75$H_2O$, respectively, and the amount of

dx.doi.org/10.1021/ic5001599 | Inorg. Chem. 2014, 53, 5961−5971

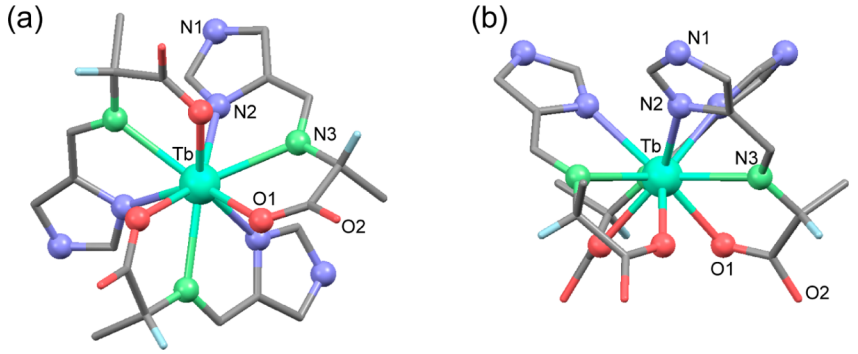

Figure 1. (a) Molecular structure of "*fac*"-[$Tb^{III}(HL^{D\text{-}ala})_3$] viewed along the C_3 axis. Hydrogen atoms except for those bound for the chiral carbon centers are omitted. Three imidazole nitrogen atoms N2 and three carboxylate oxygen atoms O1 form the two outer triangular faces, and the capping positions are occupied by three imine nitrogen atoms N3. (b) Side view.

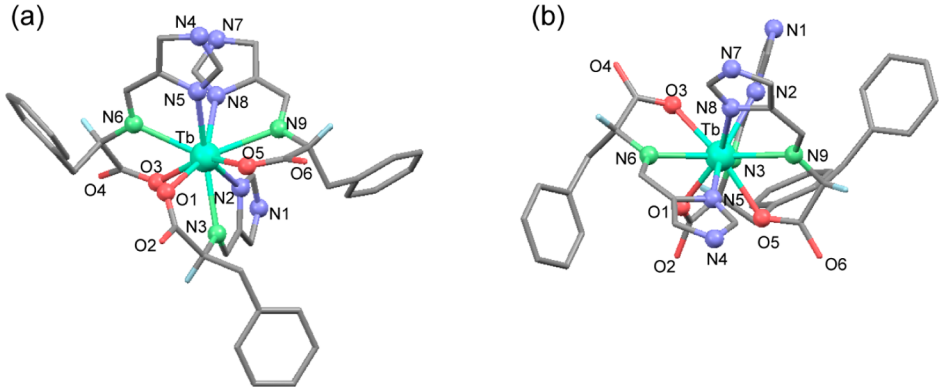

Figure 2. (a) Molecular structure of "*mer*"-[$Tb^{III}(HL^{D\text{-}phe})_2(HL^{L\text{-}phe})$] with the selected atom-numbering scheme. Hydrogen atoms except for those bound for the chiral carbon centers are omitted. (b) Side view.

crystal water molecules seems to depend slightly on the conditions where the specimens were stored and measured. IR spectra showed a sharp band at ca. 1645 cm^{-1} assignable to C═N stretching vibration of Schiff-base ligand. The strong absorptions at ca. 1590 and 1400 cm^{-1} are assigned to $\nu_a(COO^-)$ and $\nu s(COO^-)$ of the amino acid moiety, respectively.

Crystal Structures of 1 and 2. Complex **1** crystallized into a centrosymmetric trigonal space group $R\bar{3}$ (No. 148) and has a structure isomorphous to that of the corresponding Eu^{III} complex.[7] The crystallographically independent unit is one-third of "*fac*"-[$Tb^{III}(HL^{DL\text{-}ala})_3$]·$8H_2O$, consisting of one Tb^{III} ion at the special position on a C_3 rotation axis, one tridentate ligand $HL^{DL\text{-}ala}$ ($HL^{D\text{-}ala}$ or $HL^{L\text{-}ala}$) and two water molecules at the general positions, and two water molecules at the special positions. As the complex crystallized into a centrosymmetric space group and has C_3 symmetry, the crystal structure consists of two enantiomers of "*fac*"-[$Tb^{III}(HL^{D\text{-}ala})_3$] and "*fac*"-[$Tb^{III}(HL^{L\text{-}ala})_3$].

Figure 1a and 1b shows the molecular structures of "*fac*"-[$Tb^{III}(HL^{D\text{-}ala})_3$] viewed along and perpendicular to the C_3 axis (*c* axis), respectively, and molecular packing in the crystal is depicted in Figure S3 (Supporting Information). Each tridentate ligand coordinates to a Tb^{III} ion by NNO donor atoms as mononegative tridentate ligand of $HL^{D\text{-}ala}$ in which the carboxyl group of the alanine moiety is deprotonated. The complex has C_3 symmetry, and three planar unsymmetrical ONN tridentate ligands are oriented parallel to each other, showing "*facial*" configuration. Three methyl groups at the alanine moieties related by C_3 symmetry operations are well packed in "*fac*"-[$Tb^{III}(HL^{D\text{-}ala})_3$], demonstrating that "*fac*"-[$Tb^{III}(HL^{D\text{-}ala})_3$] and "*fac*"-[$Tb^{III}(HL^{L\text{-}ala})_3$] are preferable molecular geometries. The space-filling representation of "*fac*"-[$Tb^{III}(HL^{D\text{-}ala})_3$] also suggests that the species involving $HL^{D\text{-}ala}$ and $HL^{L\text{-}ala}$, that is, "*fac*"-[$Tb^{III}(HL^{D\text{-}ala})_2(HL^{L\text{-}ala})$] and "*fac*"-[$Tb^{III}(HL^{L\text{-}ala})_2(HL^{D\text{-}ala})$], are unfavorable due to the steric hindrance. The Tb^{III} ion on a 3-fold rotation axis is coordinated by N_6O_3 donor atoms of three unsymmetrical NNO tridentate ligands with $HL^{D\text{-}ala}$ or three of $HL^{L\text{-}ala}$, and the Tb^{III} complex has a saturated coordination number of nine, with one imidazole and one imine nitrogen atom (N_{het} and N_{am}, respectively) and one carboxylate oxygen atom per ligand coordinating to a Tb^{III} ion. The coordination bond distances are Tb−$N2_{het}$ (2.555(7) Å), Tb−$N3_{am}$ (2.552(8) Å), and Tb−O1 (2.373(5) Å). The coordination geometry is described as a tricapped trigonal prism (TCTP). Three N_{het} atoms generated by C_3 symmetry operations to $N2_{het}$ and three carboxylate oxygen atoms generated by C_3 symmetry operations to O1 form the two outer triangular faces, and the cap positions are occupied by three N_{am} atoms generated by C_3 symmetry operations to $N3_{am}$.

Complex **2** crystallized into a centrosymmetric tetragonal space group $I4_1/a$ (No. 88) with $Z = 16$ and has a structure isomorphous to that of the corresponding Eu^{III} complex.[7] The crystallographically independent unit consists of one "*mer*"-[$Tb^{III}(HL^{DL\text{-}phe})_3$] and 8.75 water molecules as crystal solvents. Two enantiomers related by an inversion center, "*mer*"-[$Tb^{III}(HL^{D\text{-}phe})_2(HL^{L\text{-}phe})$] and "*mer*"-[$Tb^{III}(HL^{D\text{-}phe})(HL^{L\text{-}phe})_2$], coexist in the crystal lattice. Figure 2a and 2b shows the molecular structure of "*mer*"-[$Tb^{III}(HL^{D\text{-}phe})_2(HL^{L\text{-}phe})$] involv-

dx.doi.org/10.1021/ic5001599 | *Inorg. Chem.* 2014, 53, 5961−5971

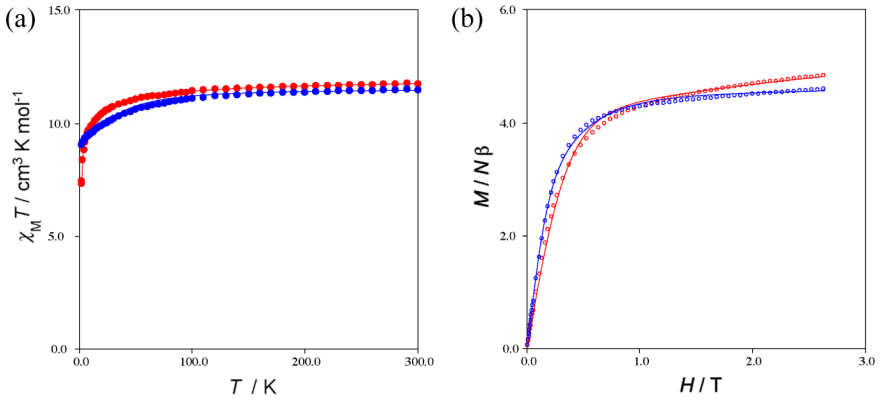

Figure 3. Plots of the (a) temperature dependence of $\chi_M T$ and (b) field dependence of $M/N\beta$ at 1.9 K for **1** (red circles) and **2** (blue circles). Solid lines represent the theoretical curves with the best-fit parameters given in the text.

ing two $HL^{D\text{-phe}}$ and one $HL^{L\text{-phe}}$ in which two of three ligands with NNO donor atoms array in the same direction and one ligand arrays in the opposite direction forming "*meridional*" configuration. The Tb^{III} ion is coordinated by N_6O_3 donor atoms of three tridentate ligands, and the coordination geometry is approximately described as the "*meridional*" configuration, two N_{het} atoms of two tridentate ligands and one carboxylate oxygen atom of one ligand (N2, N8, O3) form the one outer triangular face, two carboxylate oxygen atoms and one N_{het} atom (O1, O5, N5) form the another outer triangular face, and the cap positions are occupied by three N_{am} atoms (N3, N6, N9). The coordination geometry is described as a TCTP. It is known that all of the tris-tridentate nine-coordinate complexes have essentially the same structure; the central donor atom occupies the capping position, and the outer donor atoms occupy opposite sites in the capped quadrilateral face.[16] Three Tb−O distances are 2.364(4)−2.434(4) Å, three Tb−N_{am} distances are 2.517(5)−2.555(5) Å, and three Tb−N_{het} distances are 2.534(5)−2.569(5) Å. According to an earlier report on the isomorphous Eu^{III} complex,[7] the coordination geometry can also be described as a capped square antiprism (CSAP) in which N6 is positioned at the cap, and atoms N2, N3, O5, and N9 and atoms O1, O3, N8, and N5 occupy the upper and lower squares, respectively. The difference between them seems to be slight[16] and difficult to distinguish owing to the bond lengths and angles dependent on the atoms and their charges. The molecular arrangement in the crystal of **2** is drawn in Figure S4 (Supporting Information).

Direct Current Magnetic Properties of 1 and 2. The temperature dependences of direct current (dc) magnetic susceptibilities in the temperature range of 1.9−300 K and the field dependences of the magnetization at 1.9 K in the range 0−5 T were measured for **1** and **2**. Figure 3a shows the $\chi_M T$ vs T plot and Figure 3b the M vs H plot for **1** and **2**. The $\chi_M T$ values of **1** and **2** are 11.76 and 11.51 cm^3 K mol^{-1} at 300 K, respectively, being close to the expected values in the free ion approximation, $\chi_M T = g_J^2 N\beta^2 J(J+1)/3k_B$, i.e., 11.82 cm^3 K mol^{-1} for Tb^{III} ($4f^8$, $S = 3$, $L = 3$, $J = 6$, $g_J = 3/2$, $^7F_6$).

The $\chi_M T$ values are almost constant above 150−200 K and show a gradual decrease at lower temperatures. On lowering the temperature, the $\chi_M T$ value decreases to reach a value of 7.31 cm^3 K mol^{-1} for **1** and 9.05 cm^3 K mol^{-1} for **2** at 1.9 K. The decrease of $\chi_M T$ in the low-temperature region is due to the CF effect on the Tb^{III} ion that removes the degeneracy of the $2J+1$ components of the $^{2S+1}L_J$ ground state, $|J, J_z\rangle = |6, J_z\rangle$ ($J_z = \pm6, \pm5, \pm4, \pm3, \pm2, \pm1, 0$) for the $^7F_6$ ground state of Tb^{III}, into a series of sublevels (known as Stark splitting) whose width is on the order of 100 cm^{-1}.[9,15] Therefore, while at room temperature most sublevels are populated and the free ion value is approached, when the temperature is lowered the higher levels are depopulated and $\chi_M T$ decreases. When comparing the results on **1** and **2**, the $\chi_M T$ drop is more drastic for **1** (Figure 3a), suggesting that the ground J_z sublevel of **1** has a small J_z.

In order to quantify the magnetic anisotropy of these complexes, the temperature dependence of $\chi_M T$ and the field dependence of M were analyzed using a spin Hamiltonian approach and taking into account the crystal field (CF). A detailed analysis of the CF effect on the Ln^{III} would require diagonalization of a spin Hamiltonian,

$$\mathbf{H} = \beta(\mathbf{L}_{Ln} + 2\mathbf{S}_{Ln})H + \mathbf{H}_{cf}(Ln) \quad (1)$$

in which the CF interaction contribution is represented by the equation using the Steven's operators, $\mathbf{H}_{cf} = \sum_{k=2,4,6}\sum_{q=0}^{k} B_k^q \mathbf{O}_k^q$.[17] Although several excited states should in principle be included in magnetic analysis of lanthanide compounds, the magnetic behavior in the temperature range where only the Stark sublevels of the ground state are populated could be well reproduced considering solely the ground state components and employing the spin equivalent operator approach. Moreover, to avoid overparameterization we considered only the axial anisotropy terms, corresponding to the Stevens operators $\mathbf{O}_2^0$, $\mathbf{O}_4^0$, and $\mathbf{O}_6^0$, which can be expressed as polynomials of the total angular momentum operators $\mathbf{J}^2$ and $\mathbf{J}_z$. This choice reduces the anisotropy parameters from 15 to 3 and is justified, at least for the Tb^{III} ion, by the approximate D_{3h} CF symmetry around the lanthanide ion. Moreover, such a choice has often been employed to reproduce the magnetic behavior of Tb^{III} complexes.[3a,b,5a] The magnetic behavior was therefore analyzed with the following Hamiltonian,

$$\mathbf{H} = \beta H g_J \mathbf{J}_{Ln} + B_2^0 \mathbf{O}_2^0 + B_4^0 \mathbf{O}_4^0 + B_6^0 \mathbf{O}_6^0 \quad (2)$$

where H denotes the applied magnetic field, β is the Bohr magneton, and B_2^0, B_4^0, and B_6^0 are the axial anisotropy parameters of the Ln^{III} ion. According to the Abragam and Bleany notation, the anisotropy parameters B_k^q are related to the CF parameters, also employed in the molecular magnetism literature, by the equation $B_k^q = A_k^q \langle r^k \rangle \theta_k$, where θ_k are the Stevens coefficients.[17,18]

The temperature dependence of $\chi_M T$ for **1** and **2** in the whole temperature range was analyzed with Hamiltonian of (eq

dx.doi.org/10.1021/ic5001599 | Inorg. Chem. 2014, 53, 5961−5971

2); although several fits corresponding to a minimum of the agreement factor $R = \Sigma(\chi_M T_{obsd} - \chi_M T_{calcd})^2/\Sigma(\chi_M T_{calcd})^2$ were actually found, all with almost the same values of g_J and B_2^0 and differing mainly in the B_4^0 and B_6^0 values, the best fit compatible with the M vs H behavior and the luminescence spectra (see below) was obtained with $g_J = 1.50$, $B_2^0/k_B = 2.12$ K, $B_4^0/k_B = -0.036$ K, and $B_6^0/k_B = -4.1 \times 10^{-4}$ K for **1** and $g_J = 1.49$, $B_2^0/k_B = -1.93$ K, $B_4^0/k_B = 0.012$ K, and $B_6^0/k_B = -2.3 \times 10^{-4}$ K for **2**. The theoretical curves are shown as solid lines in Figure 3a. It is noted that the g_J values of 1.49 and 1.50 are very close to the theoretical value of 3/2 and that the sign of the leading parameter B_2^0 is opposite for **1** and **2**, leading to a completely different order of the $\pm M_J$ components. The calculated B_k^q parameters are resumed in Table 3 together with the corresponding CF parameters $A_k^q\langle r^k\rangle\theta_k$, and their values are of the same orders of magnitude of those reported for other Tb^{III} complexes.[3a,b,5a,19]

Table 3. Magnetic Anisotropy Parameters of 1 and 2 Estimated from Magnetic Analyses[a]

anisotropy parameters	1	2
g_J	1.50	1.49
B_2^0/k_B	+2.12	−1.93
$A_2^0\langle r^2\rangle/k_B$	− 210	+ 190
B_4^0/k_B	−0.036	+0.012
$A_4^0\langle r^2\rangle/k_B$	−295	+100
B_6^0/k_B	-4.1×10^{-4}	-2.3×10^{-4}
$A_6^0\langle r^2\rangle/k_B$	+380	+210

[a]All values are in Kelvin.

The diagrams of the multiplet energy levels of the Tb^{III} ions for **1** and **2** are represented in Figure 4 and show significant differences for the two complexes. First, we notice that owing to the use of a simplified spin Hamiltonian containing only axial terms, all components with the same $|M_J|$ values are degenerates, so that the sublevels originating from the splitting of the $^7F_6$ ground state of Tb^{III} under the CF effect are made up of $|\pm M_J\rangle$ pseudodoublets except $|0\rangle$. For **1** the lowest sublevel corresponds to the $|0\rangle$ component with the first excited state, $|\pm1\rangle$, at 3 cm^{-1} and the highest pseudodoublet, a $|\pm6\rangle$, at 209 cm^{-1}, which defines the total Stark splitting. Such an energy level pattern indicates an easy-plane anisotropy of the Tb^{III} ion, in agreement with experimental evidence showing the lack of out of phase signal in the ac magnetic susceptibility (vide infra). For **2**, on the other hand, the lowest sublevel corresponds to the $|\pm6\rangle$ pseudodoublet with the first excited state, $|\pm4\rangle$, at 6 cm^{-1} and the highest sublevel, $|0\rangle$, significantly mixed with $|\pm2\rangle$, at 210 cm^{-1}, which defines the total Stark splitting. Such an energy level pattern indicates an easy-axis (Ising type) anisotropy of the Tb^{III} ion.

The field dependences of the magnetization from 0 to 5 T for **1** and **2** are shown in Figure 3b. Upon increasing the applied external magnetic field, the magnetization of both Tb^{III} complexes increases to 4.85 $N\beta$ for **1** and 4.61 $N\beta$ for **2** at 5 T without reaching the expected saturation value of $9N\beta$. This is again due to the CF effect on the Tb^{III} ion ($4f^8$, $J = 6$, $S = 3$, $L = 3$, $^7F_6$) that removes the 13-fold degeneracy of the $^7F_6$ ground state. Reasonable agreement is observed between the curves obtained with the Hamiltonian of eq 2 and the same parameters obtained from the fit of magnetic susceptibilities, see solid lines in Figure 3b, although accurate fits require an adjustment of the B_2^0, B_4^0, and B_6^0 parameters leading to $B_2^0/k_B = 2.03$ K, $B_4^0/k_B = -0.023$ K, and $B_6^0/k_B = -2.9 \times 10^{-4}$ K for **1** and $g_J = 1.49$, $B_2^0/k_B = -1.82$ K, $B_4^0/k_B = 0.019$ K, and $B_6^0/k_B = -1.3 \times 10^{-4}$ K for **2**.

Luminescent Properties of 1 and 2. Figure 5a shows the photograph of the solid samples of **1** and **2** at room temperature under irradiation of UV light (254 nm). Efficient f−f emissions were observed, and the emission quantum yields in the solid state at room temperature were determined to be as high as $\Phi = 0.50$ and 0.61 for **1** and **2**, respectively. The additional aromatic ring in $HL^{DL\text{-}phe}$ of **2** may play a better role in the antenna effect.

Figure 5b and 5c shows the f−f emission spectra of **1** and **2** recorded in the solid state at 77 K upon irradiation of UV light at 291 and 301 nm, respectively. Emission bands were clearly found at ca. 490, 545, 585, and 620 nm for both complexes and attributed to the f−f transition $^5D_4 \rightarrow {}^7F_J$ with $J = 6$, 5, 4, and 3, respectively. Emission bands attributable to the f−f transition $^5D_4 \rightarrow {}^7F_J$ with $J = 2$, 1, and 0 were weakly observed at ca. 650, 665, and 675 nm, respectively. Each band exhibited a fine structure with several peaks. The fine structures of the emission bands at 490 nm for **1** and **2** show different spectral patterns. For **1** the $^5D_4 \rightarrow {}^7F_6$ transition shows two broad peaks at 488.5 and 490.7 nm, and deconvolution of the spectrum indicates four components at 20.517×10^3, 20.471×10^3, 20.383×10^3, and 20.315×10^3 cm^{-1}. For **2** the $^5D_4 \rightarrow {}^7F_6$ transition shows a broad peak at 489.8 nm with two wide shoulders at 487.5 and 492.4 nm, and deconvolution of the spectrum indicates three main components at 20.514×10^3, 20.416×10^3, and 20.291×10^3 cm^{-1}. The emission spectrum involves information on the

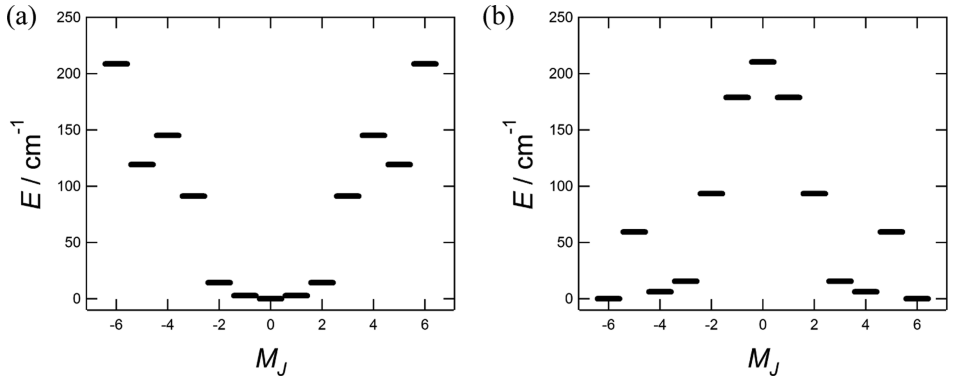

Figure 4. Energy levels of the ground state $^7F_6$ multiplets for the Tb^{III} ion in (a) **1** and (b) **2** obtained from magnetic analysis.

dx.doi.org/10.1021/ic5001599 | Inorg. Chem. 2014, 53, 5961−5971

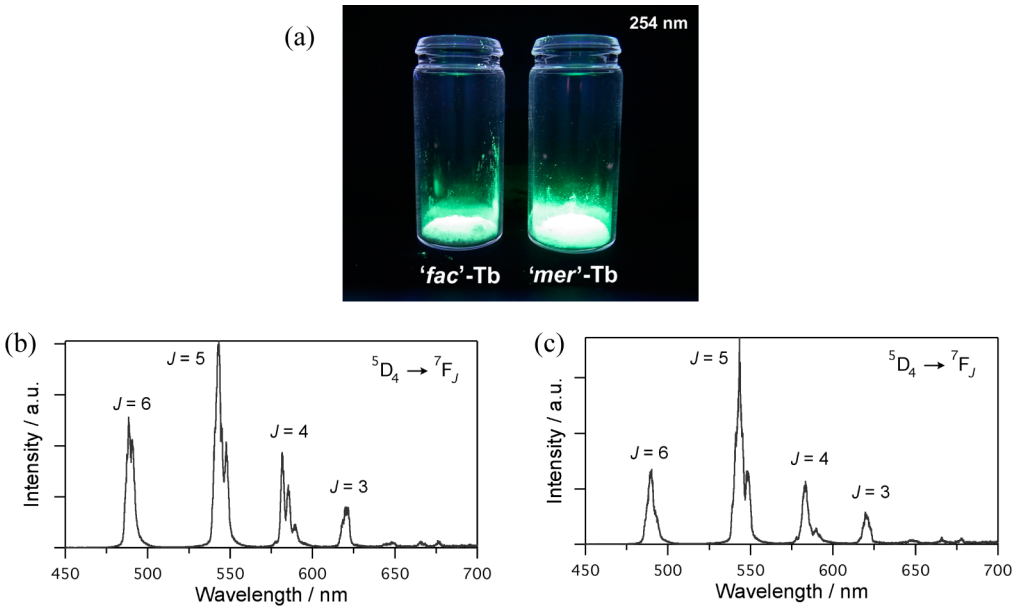

Figure 5. (a) Photograph of the solid samples of **1** ("*fac*"-Tb) and **2** ("*mer*"-Tb) at room temperature under irradiation of UV light (254 nm). Emission spectra of a solid-state sample of (b) **1** by irradiation at 291 nm and (c) **2** by irradiation at 301 nm recorded at 77 K.

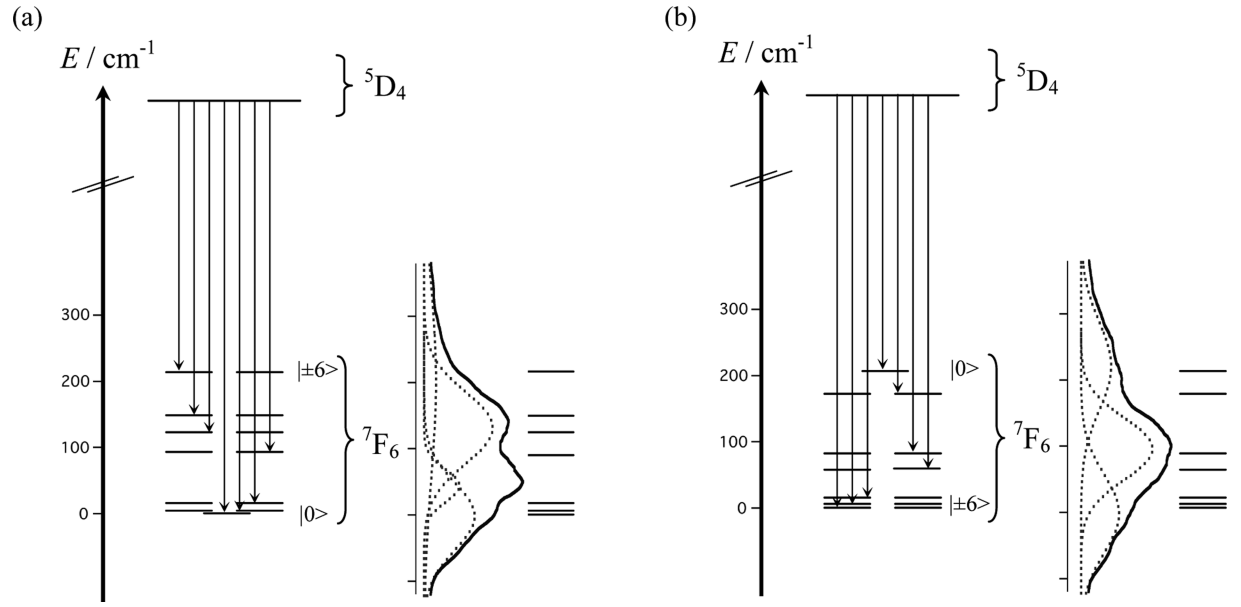

Figure 6. Comparison of the Stark splitting of the $^7F_6$ ground state of the Tb^{III} ions from magnetic analysis (left) and the splitting observed from the emission f–f spectrum (on the right) for (a) **1** and (b) **2**. Deconvolution results are superposed on the right.

ground state Stark multiplet originating from the $^7F_6$ state. The highest energy peak of the band corresponds to the transition to the lowest sublevel.

The splitting observed from the emission can be directly compared with the energy diagram obtained from fitting of the magnetic susceptibility measurements. The comparison for **1** is illustrated in Figure 6a and allows us to assign the four components of the $^5D_4 \rightarrow {}^7F_6$ band to superpositions of transitions from the excited $^5D_4$ state to four groups of sublevels close in energy, namely, $|0\rangle$, $|\pm1\rangle$, $|\pm2\rangle$ for the peak at 20.517×10^3 cm^{-1}, $|\pm3\rangle$ for the peak at 20.471×10^3 cm^{-1}, $|\pm4\rangle$, $|\pm5\rangle$ for the peak at 20.383×10^3 cm^{-1}, and $|\pm6\rangle$ for the peak at 20.315×10^3 cm^{-1}. Indeed, the calculated splitting between these four groups of sublevels, ca. 60–70, 130–140, and 190–200 cm^{-1}, fits fairly well to the observed energy differences between the four emission peaks they are assigned to (46, 134, and 202 cm^{-1} above the lowest line at 20.517×10^3 cm^{-1}). The highest emission peak (20.315×10^3 cm^{-1}) is characterized to be somewhat broad and weak, probably because it is mostly buried with the other emission peaks owing to the limit of the present spectral resolution. Peak broadening is attributed partly to the presence of a few phases with various *n* hydrations in $[Tb^{III}(HL^{DL\text{-}ala})_3]\cdot nH_2O$.

The comparison for **2** is illustrated in Figure 6b and allows us to assign the three main peaks of the $^5D_4 \rightarrow {}^7F_6$ band to superpositions of transitions from the excited $^5D_4$ state to three groups of sublevels close in energy, namely, $|\pm6\rangle$, $|\pm4\rangle$, $|\pm3\rangle$ for the peak at 20.514×10^3 cm^{-1}, $|\pm5\rangle$, $|\pm2\rangle$ for the peak at 20.416×10^3 cm^{-1}, and $|\pm1\rangle$, $|0\rangle$ for the peak at 20.291×10^3 cm^{-1}. The calculated energy difference between these three

dx.doi.org/10.1021/ic5001599 | *Inorg. Chem.* 2014, 53, 5961–5971

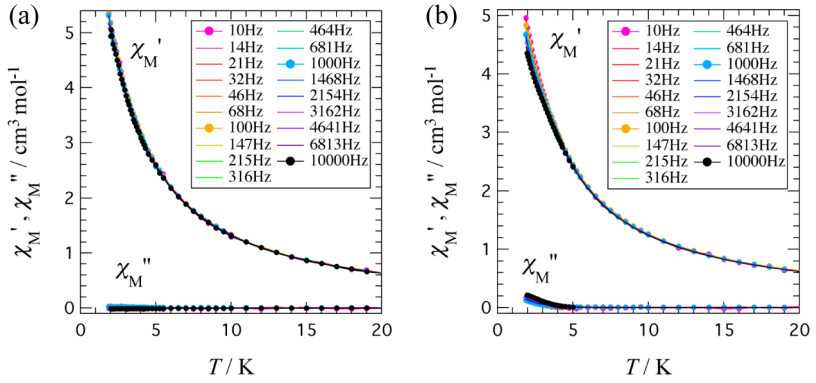

Figure 7. Temperature dependences of the in-phase (χ_M') and out-of phase (χ_M'') ac susceptibility signals of (a) **1** and (b) **2** measured at a 5 Oe ac field of various frequencies and a 1000 Oe external dc field.

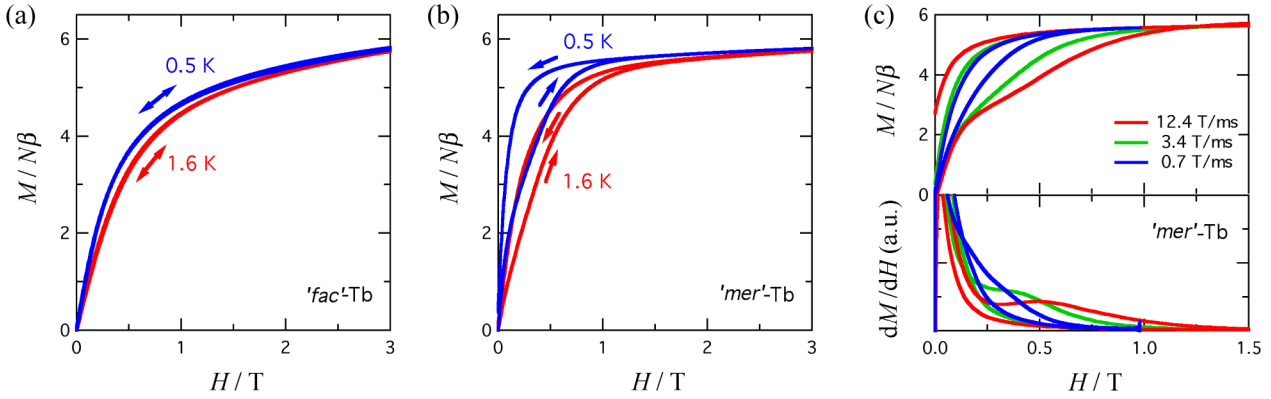

Figure 8. Pulsed-field magnetizations for (a) **1** and (b) **2** measured at 0.5 and 1.6 K. (c) Sweep-rate dependence of the magnetization of **2** measured at 0.5 K. The corresponding dM/dH vs H plot is also shown in the bottom panel.

groups of sublevels, ca. 80−90 and 200 cm^{-1}, fits reasonably well the observed energy difference between the three emission peaks they are assigned to (98 and 223 cm^{-1} above the lowest line at 20.514 × 10^3 cm^{-1}). The agreement between magnetic and fluorescence properties is quite good for both **1** and **2** and supports the proposed Stark splitting of the J_z sublevels of the Tb^{III} ion and the nature of the magnetic anisotropy. The emission spectra of **1** and **2** measured at room temperature are shown in Figure S5 (Supporting Information). No appreciable temperature-dependent band (hot band)[20] could be detected within the present resolution.

Alternating Current Magnetic Properties of 1 and 2. The magnetization dynamics behavior and possibility of a SIM character were investigated for **1** and **2** by means of the ac magnetic susceptometry down to 1.9 K. At zero bias field, the in-phase (χ_M') and out-of-phase (χ_M'') components exhibit no frequency dependence (Figure S6, Supporting Information). With the application of an external dc bias field of 1000 Oe, while **1** showed no frequency dependence either (Figure 7a), **2** exhibited an onset of χ_M'' and frequency dependence around 2 K (Figure 7b), an indication of SIM behavior.

No peak was found in χ_M'' above 1.9 K up to 10 kHz for **2**. To estimate the activation energy (Δ) for the magnetization reorientation, Arrhenius analysis was attempted, including a modified $\ln(\chi_M''/\chi_M')$ vs T^{-1} plot[21] (Figure S7, Supporting Information). The activation energy for the magnetization reorientation Δ and pre-exponential factor τ_0 are defined as $\ln(\chi_M''/\chi_M') = \ln(\omega\tau_0) + \Delta/k_BT$. A linear fit can be applied in a narrow temperature region, giving rise to a relatively large deviation error. We roughly estimated Δ/k_B = 2.7(4) K and τ_0 = 5(2) × 10^{-7} s. The small Δ is responsible for the low blocking temperature, which may be located much below 2 K.

Now we can confirm that the prediction from the energy diagrams based on the CF calculation (Figure 4) is realized in the ac magnetic susceptibility measurements, that is, the magnetic easy-plane anisotropy is suggested by an approximate single-well potential curve for **1**, and **1** does not behave as a SIM above 1.9 K. On the other hand, the easy-axis anisotropy is expected from a double-well- or quadruple-well-type curve for **2**, and **2** actually exhibited an indication of a SIM behavior around 2 K. However, from a quantitative analysis, the activation energy observed (2.7(4) K) is considerably smaller than that of the full thermal barrier from CF calculation (210 cm^{-1}). The observed dynamics may be related to a phonon-assisted tunneling relaxation process with a dominant contribution from the first excited doublet, $|\pm4\rangle$, at only 6 cm^{-1}. The lowest energy levels are $|\pm6\rangle$, and a trigonal symmetry of the Tb ion in **2** would favor a direct relaxation process between $|+6\rangle$ and $|-6\rangle$, consistent with the small effective activation energy for the magnetization reorientation for **2**.

Pulsed-Field Magnetization of 1 and 2. From Figure 3b we find a very small slope at around 7 T in the magnetization curve of **2**, consistent with the relatively strong magnetic anisotropy of **2** expected from the energy diagram described above. However, no hysteresis behavior was found in the SQUID time-scale above 1.9 K. Pulsed-field magnetization experiments afforded unequivocal evidence for characterization of **2** as a SIM. Figure 8a and 8b shows the magnetization curves of powder specimens of **1** and **2**, respectively, measured at 1.6

dx.doi.org/10.1021/ic5001599 | Inorg. Chem. 2014, 53, 5961−5971

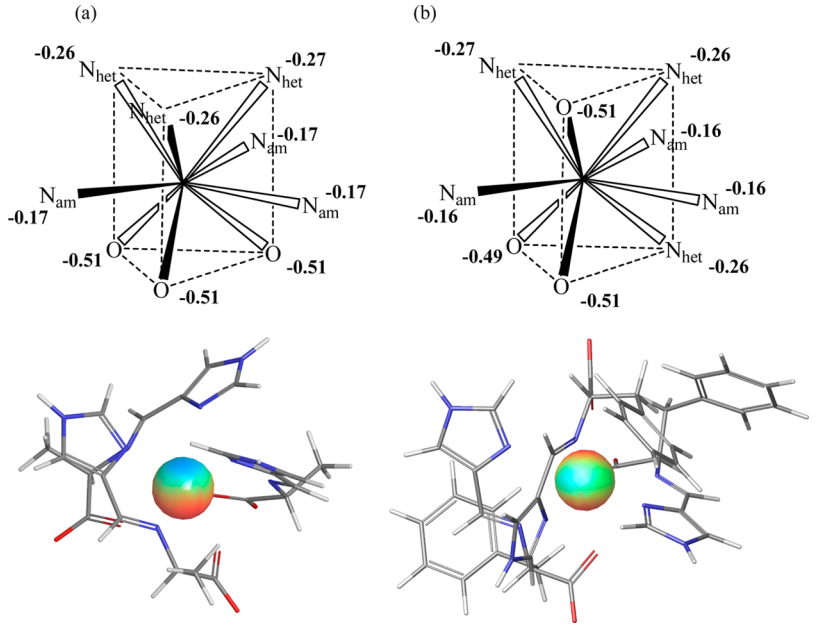

Figure 9. (Top) Mulliken charges of the O and N donor atoms, and (bottom) ligand electrostatic potential projected on a sphere of radius 2 Å centered in the Tb^{III} ion position for (a) **1** and (b) **2**. Red and blue colors correspond, respectively, to a more negative and less negative electrostatic potential.

and 0.5 K. Compound **1** did not behave as a SIM even at 0.5 K, whereas **2** exhibited magnetic hysteresis, suggesting the presence of the activation barrier of magnetization reversal only for **2**. This finding agrees well with the ac susceptibility results (Figure 7a and 7b) and the energy diagram proposed (Figure 4). Furthermore, the field position of the magnetization upsurge for **2** depends on the temperature. Figure 8c displays the wider hysteresis loop upon the faster field sweep. The fields where dM/dH reaches maximum are 0.50, 0.35, and ca. 0.2 T for rates of 12.4, 3.4, and 0.7 T/ms, respectively. Relaxation occurs via a thermal activation mechanism. Thus, **2** is characterized to be a SIM due to slow magnetization reorientation.

There have recently been several reports on observing slow relaxation of the magnetization for easy-plane lanthanide ion systems.[22] Relaxation behavior is supposed to involve some different mechanisms, such as the direct process (which contributes to τ^{-1} with a term proportional to T), the Raman process (proportional to T^n), the Orbach process (proportional to $\exp(-\Delta/k_BT)$), and quantum tunneling. Arrhenius parameters obtained here have empirical meaning and do not necessarily guarantee that the present barrier Δ is the only driving force for the slow relaxation. Compound **2** has Tb^{3+}, an ion favorable for the axial anisotropy, and it is likely that the slow relaxation is attributed to the double-well energy level pattern (Figure 4b). Compound **1** is not a SIM, being compatible with the absence of Δ (Figure 4a). Even though the possibility of other relaxation mechanisms is taken into consideration, it is safely concluded that any slow relaxation process would not be operative above 0.5 K.

DFT Calculations on 1 and 2. In order to point out the reason behind the different magnetic behavior and Stark splitting pattern of **1** and **2**, showing an easy-plane character for **1** and an easy-axis character for **2**, we performed DFT calculation on the ligand environment aiming at estimating the electrostatic potential acting on the Tb^{III} ion that is responsible for the CF acting on it. Indeed, the CF acting on a lanthanide ion determines the kind and strength of its magnetic anisotropy, and in particular, strong easy-axis anisotropy is achieved when the CF stabilizes the ground sublevels with the highest $|M_J\rangle$ values of the $^7F_6$ ground state of Tb^{III}. These sublevels, in particular $|\pm6\rangle$, are known to have oblate spheroidal electronic distribution (that is, they have a larger electron distribution on the equatorial plane than on the principal axis) and therefore expected to be stabilized by CFs originating from a ligand negative charge distribution with dipolar character, i.e., with large negative charges from the donor atoms located around the principal axis, leading to easy-axis anisotropy.[23]

DFT calculation with the UB3LYP-D3 functional was carried out on the ligands environment, excluding the Tb^{III} ion, using the geometry from X-ray analysis, and the resulting Mulliken analysis is reported in Figure 9 together with the corresponding molecular electrostatic potential acting on the Tb ion. Figure 9a clearly shows that the negative charges on the carboxylate oxygen are significantly larger than those on the imine and imidazole nitrogen atoms by 0.14−0.24 *e* units, and therefore, their position will determine the anisotropy of the negative charge distribution. We notice that while in the "*fac*" isomer **1** the largest negative charges on O atoms are located on the same triangle of the TCTP coordination sphere, in the "*mer*" isomer **2** two of the largest negative charges on O atoms are located on a basal triangle and the remaining one on the opposite triangle. Figure 9b shows the consequence of these different charge arrangements on the electrostatic potential on a sphere of radius 2 Å centered in the Tb position. In both cases there is a small less negative electrostatic region originating from the neutral ligands (amine and imidazole nitrogens) and a more negative region originating from the negative ligands (carboxylate oxygens); however, while for the "*fac*" isomer **1** two regions of high (red) and low (blue) electrostatic potential are located on opposite sides of the sphere around the Tb^{III} ion, for the "*mer*" isomer **2** the region of high (red) electrostatic potential is more spread on the

dx.doi.org/10.1021/ic5001599 | *Inorg. Chem.* 2014, 53, 5961−5971

sphere and partially located on opposite sides. For **1**, therefore, the region of high negative potential is located on only one side, indicating no particular stabilization of the $|\pm6\rangle$ sublevel and possibly a magnetic easy-plane character. On the other hand, for **2**, the electrostatic potential has a more dipolar character, indicating stabilization of the $|\pm6\rangle$ sublevel and therefore magnetic easy-axis character. The high electrostatic potential regions are, however, not well separated by a low potential in the equatorial region (due to the meridional arrangement of the three negative charges on O), so that the stabilization of the $|\pm6\rangle$ sublevel is expected to be small and the anisotropy is weak, consistent with the low activation energy observed for the magnetization reorientation.

These results indicate that careful analysis of the negative charge distribution around the Tb^{III} ion from DFT calculations allows one to give a rationale for the different behavior of the "*fac*" and "*mer*" isomers, showing how changes of the coordination geometry of the same ligand may have large consequences on the ac magnetic behavior of the corresponding complexes.

CONCLUSION

The present work provides a mononuclear Tb^{III} complex with multifunctionality, namely, **2**, which is a potential SIM with an efficient luminescent property. The Tb^{III}–HL^{aa} system affords two contrasting types of complexes: the easy-plane and -axis magnetic anisotropies for aa = DL-ala and DL-phe, respectively. The luminescence fine structure assignable to the $^5D_4 \rightarrow {}^7F_6$ transition is in good accordance with the energy diagram determined from magnetic analysis. The energy diagram of **1** shows an approximate single-well potential curve, whereas that of **2** shows a quadruple-well potential curve, within the $^7F_6$ multiplets. Accordingly, complex **2** displayed an onset of the out-of-phase signal in ac susceptibility, but **1** did not. The magnetic hysteresis of **2** was recorded in the pulsed-field magnetization measurements. DFT calculation allowed us to estimate the negative charge distribution around the Tb^{III} ion, giving a rationale to the different magnetic anisotropies of **1** and **2**. Application of the present strategy to other lanthanide ions is now in progress.

ASSOCIATED CONTENT

Supporting Information

TGA results, molecular packing diagrams, temperature and frequency dependences of the ac magnetic susceptibilities at 0 dc bias field, and X-ray crystallographic files (CIF) for **1** and **2**. This material is available free of charge via the Internet at http://pubs.acs.org. X-ray crystallographic data in CIF format have been deposited with CCDC (reference numbers CCDC 976923 and 976924). They can be obtained free of charge via http://www.ccdc.cam.ac.uk/conts/retrieving.html or from the Cambridge Crystallographic Data Centre, 12 Union Road, Cambridge CB2 1EZ, UK; fax (+44) 1223-336-033 or e-mail deposit@ccdc.cam.ac.uk.

AUTHOR INFORMATION

Corresponding Authors

*E-mail: naohide@aster.sci.kumamoto-u.ac.jp.
*E-mail: ishi@pc.uec.ac.jp.

Notes

The authors declare no competing financial interest.

ACKNOWLEDGMENTS

Part of this work was performed under the Interuniversity Cooperative Research Program of the Institute for Materials Research, Tohoku University (Proposal No. 13K0089). T.F. was supported by the Research Fellowship of the Japan Society for the Promotion of Science, KAKENHI 00248498.

REFERENCES

(1) (a) Sessoli, R.; Gatteschi, D.; Caneschi, A.; Novak, M. A. *Nature* **1993**, *365*, 141−143. (b) Gatteschi, D.; Caneschi, A.; Pardi, L.; Sessoli, R. *Science* **1994**, *265*, 1054−1058. (c) Sessoli, R.; Tsai, H. L.; Schake, A. R.; Wang, S.; Vincent, J. B.; Folting, K.; Gatteschi, D.; Christou, G.; Hendrickson, D. N. *J. Am. Chem. Soc.* **1993**, *115*, 1804−1816. (d) Thomas, L.; Lionti, F.; Ballou, R.; Gatteschi, D.; Sessoli, R.; Barbara, B. *Nature* **1996**, *383*, 145−147. (e) Boskovic, C.; Brechin, E. K.; Streib, W. E.; Folting, K.; Bollinger, J. C.; Hendrickson, D. N.; Christou, G. *J. Am. Chem. Soc.* **2002**, *124*, 3725−3736.

(2) (a) Gatteschi, D.; Sessoli, R. *Angew.Chem., Int. Ed.* **2003**, *42*, 268−297. (b) Christou, G. *Polyhedron* **2005**, *24*, 2065−2075. (c) Gatteschi, D.; Sessoli, R.; Villain, J. *Molecular Nanomagnets*; Oxford University Press: Oxford, U.K., 2006. (d) Bagai, R.; Christou, G. *Chem. Soc. Rev.* **2009**, *38*, 1011−1026.

(3) (a) Ishikawa, N.; Sugita, M.; Ishikawa, T.; Koshihara, S.; Kaizu, Y. *J. Am. Chem. Soc.* **2003**, *125*, 8694−8695. (b) Ishikawa, N.; Sugita, M.; Okubo, T.; Tanaka, N.; Iino, T.; Kaizu, Y. *Inorg. Chem.* **2003**, *42*, 2440−2446. (c) Ishikawa, N.; Mizuno, Y.; Takamatsu, S.; Ishikawa, T.; Koshihara, S. Y. *Inorg. Chem.* **2008**, *47*, 10217−10219. (d) Woodruff, D. N.; Winpenny, R. E. P.; Layfield, R. A. *Chem. Rev.* **2013**, *113*, 5110−5148. (e) Habib, F.; Murigesu, M. *Chem. Soc. Rev.* **2013**, *42*, 3278−3288. (f) Zhang, P.; Guo, Y.-N.; Tang, J. *Coord. Chem. Rev.* **2013**, *257*, 1728−1763.

(4) (a) Osa, S.; Kido, T.; Matsumoto, N.; Re, N.; Pochaba, A.; Mronzinski, J. *J. Am. Chem. Soc.* **2004**, *126*, 420−421. (b) Hamamatsu, T.; Yabe, K.; Towatari, M.; Matsumoto, N.; Re, N.; Pochaba, A.; Mrozinski, J. *Bull. Chem. Soc. Jpn.* **2007**, *80*, 523−529. (c) Costes, J.-P.; Dahan, F.; Wernsdorfer, W. *Inorg. Chem.* **2006**, *45*, 5−7. (d) Ferbinteanu, M.; Kajiwara, T.; Choi, K. Y.; Nojiri, H.; Nakamoto, A.; Kojima, N.; Cimpoesu, F.; Fujimura, Y.; Takaishi, S.; Yamashita, M. *J. Am. Chem. Soc.* **2006**, *128*, 9008−9009. (e) Mori, F.; Nyui, T.; Ishida, T.; Nogami, T.; Choi, K.-Y.; Nojiri, H. *J. Am. Chem. Soc.* **2006**, *128*, 14408−14009. (f) Ishida, T.; Watanabe, R.; Fujiwara, K.; Okazawa, A.; Kojima, N.; Tanaka, G.; Yoshii, S.; Noriji, H. *Dalton Trans.* **2012**, *41*, 13609−13619. (g) Gao, Y.; Zhao, L.; Xu, X.; Xu, G.-F.; Guo, Y.-N.; Tang, J.; Liu, Z. *Inorg. Chem.* **2011**, *50*, 1304−1308. (h) Colacio, E.; Ruiz, J.; Mota, A. J.; Palacios, M. A.; Cremades, E.; Ruiz, E.; White, F. J.; Euan K. Brechin, E. K. *Inorg. Chem.* **2012**, *51*, 5857−5868. (i) Efthymiou, C. G.; Stamatatos, T. C.; Papatriantafyllopoulou, C.; Tasiopoulos, A. J.; Wernsdorfer, W.; Perlepes, S. P.; Christou, G. *Inorg. Chem.* **2010**, *49*, 9737−9739. (j) Burrow, C. E.; Burchell, T. J.; Lin, P.-H.; Habib, F.; Wernsdorfer, W.; Clérac, R.; Murugesu, M. *Inorg. Chem.* **2009**, *48*, 8051−8053. (k) Yamaguchi, T.; Sunatsuki, Y.; Ishida, H.; Kojima, M.; Akashi, H.; Re, N.; Matsumoto, N.; Pochaba, A.; Mrozinski, J. *Bull. Chem. Soc. Jpn.* **2008**, *81*, 598−605. (l) Hamamatsu, T.; Yabe, K.; Towatari, M.; Osa, S.; Matsumoto, N.; Re, N.; Pochaba, A.; Mrozinski, J.; Gallani, J. L.; Barla, A.; Imperia, P.; Paulsen, C.; Kappler, J. P. *Inorg. Chem.* **2007**, *46*, 4458−4468. (m) Sessoli, R.; Powell, A. K. *Coord. Chem. Rev.* **2009**, *253*, 2328−2341. (n) Costes, J. P.; Vendier, L.; Wernsdorfer, W. *Dalton Trans.* **2011**, *40*, 1700−1706. (o) Sakamoto, S.; Fujinami, T.; Nishi, K.; Matsumoto, N.; Mochida, N.; Ishida, T.; Sunatsuki, Y.; Re, N. *Inorg. Chem.* **2013**, *52*, 7218−7229.

(5) (a) Sorace, L.; Benelli, C.; Gatteschi, D. *Chem. Soc. Rev.* **2011**, *40*, 3092−3104. (b) Layfield, R. A.; McDouall, J. J. W.; Sulway, S. A.; Tuna, F.; Collison, D.; Winpenny, R. E. P. *Chem.—Eur. J.* **2010**, *16*, 4442−4446. (c) Long, J.; Habib, F.; Lin, P.-H.; Korobkov, I.; Enright, G.; Ungur, L.; Wernsdorfer, W.; Chibotaru, L.; Murugesu, M. *J. Am. Chem. Soc.* **2011**, *133*, 5319−5328. (d) Guo, Y.-N.; Xu, G.-F.; Guo, Y.; Tang, J. *Dalton Trans.* **2011**, *40*, 9953−9963. (e) Hewitt, I. J.; Tang, J.;

Madhu, N. T.; Anson, C. E.; Lan, Y.; Luzon, Y.; Etienne, M.; Sessoli, R.; Powell, A. K. *Angew. Chem., Int. Ed.* **2010**, *49*, 6352−6356. (f) Blagg, R. J.; Muryn, C. A.; McInnes, E. J. L.; Tuna, F.; Winpenny, R. E. P. *Angew. Chem., Int. Ed.* **2011**, *50*, 6530−6533. (g) Rhinehart, J. D.; Feng, M.; Evans, W. J.; Long, J. R. *J. Am. Chem. Soc.* **2011**, *133*, 14236−14239. (h) Zhang, P.; Guo, Y.-N.; Tang, J. *Coord. Chem. Rev.* **2013**, *257*, 1728−1763. (i) Luzon, J.; Sessoli, R. *Dalton Trans.* **2012**, *41*, 13556−13567. (j) Karbowiak, M.; Rudowicz, C.; Ishida, T. *Inorg. Chem.* **2013**, *52*, 13199−13206.

(6) (a) Lin, P.-H.; Burchell, T. J.; Clerac, R.; Murugesu, M. *Angew. Chem., Int. Ed.* **2008**, *47*, 8848−8851. (b) Hewitt, I. J.; Lan, Y.; Anson, C. E.; Luzon, J.; Sessoli, R.; Powell, A. K. *Chem. Commun.* **2009**, 6765−6767. (c) Guo, Y.-N.; Xu, G.-F.; Wernsdorfer, W.; Ungur, L.; Guo, Y.; Tang, J.; Zhang, H.-J.; Chibotaru, L. F.; Powell, A. K. *J. Am. Chem. Soc.* **2011**, *133*, 11948−11951. (d) Zhang, P.; Zhang, L.; Lin, S.-Y.; Tang, J. *Inorg. Chem.* **2013**, *52*, 6595−6602.

(7) Yamauchi, S.; Hashibe, T.; Murase, M.; Hagiwara, H.; Matsumoto, N.; Tsuchimoto, M. *Polyhedron* **2013**, *49*, 105−112.

(8) (a) Iihoshi, T.; Sato, T.; Towatari, M.; Matsumoto, N.; Kojima, M. *Bull. Chem. Soc. Jpn.* **2009**, *82*, 458−466. (b) Oishi, T.; Hashibe, T.; Takahashi, S.; Hagiwara, H.; Matsumoto, N.; Sunatsuki, Y. *Polyhedron* **2012**, *33*, 209−217.

(9) Kahn, O. *Molecular Magnetism*; VCH: Weinhein, 1993; Chapter 1, Table I.1.

(10) Nojiri, H.; Choi, K.-Y.; Kitamura, N. *J. Magn. Magn. Mater.* **2007**, *310*, 1468−1472.

(11) (a) SIR92: Altomare, A.; Cascarano, G.; Giacovazzo, C.; Guagliardi, A.; Burla, M.; Polidori, G.; Camalli, M. *J. Appl. Crystallogr.* **1994**, *27*, 435−436. (b) DIRDIF-99: Beurskens, P. T.; Admiraal, G.; Beurskens, G.; Bosman, W. P.; de Gelder, R.; Israel, R.; Smits, J. M. M. The DIRDIF-99 program system. *Technical Report of the Crystallography Laboratory*; University of Nijmegen: The Netherlands, 1999.

(12) *CrystalStructure 4.0: Crystal Structure Analysis Package*; Rigaku Corp.: Tokyo, Japan, 2000−2010.

(13) *Jaguar*, version 7.9; Schrödinger, LLC: New York, 2011.

(14) (a) Grimme, S.; Antony, J.; Ehrlich, S.; Krieg, H. *J. Chem. Phys.* **2010**, *132*, 154104 (19 pages). (b) Grimme, S. *J. Comput. Chem.* **2006**, *27*, 1787−1799.

(15) Cundari, T. R.; Stevens, W. J. *J. Chem. Phys.* **1993**, *98*, 5555−5565.

(16) Drew, M. G. B. *Coord. Chem. Rev.* **1977**, *24*, 179−275.

(17) Abragam, A.; Bleaney, B. *Electron Paramagnetic Resonance*; Clarendon Press: Oxford, 1970.

(18) Stevens, K. W. H. *Proc. Phys. Soc.* **1952**, *A65*, 209−215.

(19) (a) Yamaguchi, T.; Sunatsuki, Y.; Ishida, H.; Kojima, M.; Akashi, H.; Re, N.; Matsumoto, N.; Pochaba, A.; Mrozinski, J. *Inorg. Chem.* **2008**, *47*, 5736−5745. (b) Kajiwara, T.; Nakano, M.; Takaishi, S.; Yamashita, M. *Inorg.Chem.* **2008**, *47*, 8604−8606. (c) Kajiwara, T.; Takahashi, K.; Hiraizumi, T.; Takaishi, S.; Yamashita, M. *CrystEngComm* **2009**, *11*, 2110−2116. (d) Kajiwara, T.; Nakano, M.; Takahashi, K.; Takaishi, S.; Yamashita, M. *Chem.—Eur. J.* **2011**, *17*, 196−205. (e) Ehama, K.; Ohmichi, Y.; Sakamoto, S.; Fujinami, T.; Matsumoto, N.; Mochida, N.; Ishida, T.; Sunatsuki, Y.; Tsuchimoto, M.; Re, N. *Inorg. Chem.* **2013**, *52*, 12828−12841. (f) Yamashita, K.; Miyazaki, R.; Kataoka, Y.; Nakanishi, T.; Hasegawa, Y.; Nakano, M.; Yamamura, T.; Kajiwara, T. *Dalton Trans.* **2013**, *42*, 1987−1990. (g) AlDamen, M. A.; Cardona-Serra, S.; Clemente-Juan, J. M.; Coronado, E.; Gaita-Ariño, A.; Martì-Gastaldo, C.; Luis, F.; Montero, O. *Inorg. Chem.* **2009**, *48*, 3467−3479. (h) Chandrasekhar, V.; Bag, P.; Speldrich, M.; van Leusen, J.; Kögerler, P. *Inorg. Chem.* **2013**, *52*, 5035−5044.

(20) Gruber, J. B.; Nash, K. L.; Yow, R. M.; Sardar, D. K.; Valiev, U. V.; Uzokov, A. A.; Burdick, G. W. *J. Lumin.* **2008**, *128*, 1271−1284.

(21) Bartolomé, J.; Filoti, G.; Kuncser, V.; Schinteie, G.; Mereacre, V.; Anson, C. E.; Powell, A. K.; Prodius, D.; Turta, C. *Phys. Rev. B* **2009**, *80*, 014430 (16 pages).

(22) Liu, J.-L.; Yuan, K.; Leng, J.-D.; Ungur, L.; Wernsdorfer, W.; Guo, F.-S.; Chibotaru, L. F.; Tong, M.-L. *Inorg. Chem.* **2012**, *51*, 8538−8544. Lucaccini, E.; Sorace, L.; Perfetti, M.; Costes, J.-P.; Sessoli, R. *Chem. Commun.* **2014**, *50*, 1648−1651.

(23) (a) Sievers, J. *Z. Phys. B: Condens. Matter Quanta* **1982**, *45*, 2689−296. (b) Schmitt, D. *J. Phys. (Paris)* **1986**, *47*, 677−681. (c) Rinehart, J. D.; Long, J. R. *Chem. Sci.* **2011**, *2*, 2078−2085. (d) Aravena, D.; Ruiz, E. *Inorg. Chem.* **2013**, *52*, 13770−13778. (e) Chilton, N. F.; Collison, D.; McInnes, E. J. L.; Winpenny, R. E. P.; Soncini, A. *Nat. Commun.* **2013**, *4*, 2551 (7 pages).